POLITECNICO DI TORINO
Repository ISTITUZIONALE

Improved lithology prediction in channelized reservoirs by integrating stratigraphic forward modelling: towards improved model calibration in a case study of the Holocene Rhine-

(Article begins on next page)

25 April 2024

1 **Improved lithology prediction in channelized reservoirs by integrating stratigraphic forward**

2 **modelling: towards improved model calibration in a case study of the Holocene Rhine-Meuse**

3 **fluvio-deltaic system**[*]

4

5 Costanzo Peter [a,1] costanzo.peter@polito.it (Corresponding author)

6 Eloisa Salina Borello [a,2] eloisa.salinaborello@polito.it

7 Rory A.F. Dalman [b,3] rory.dalman@tno.nl

8 Pantelis Karamitopoulos [c,4] pkaramitopoulos@gmail.com

9 Freek Busschers [b,5] freek.busschers @tno.nl

10 Quinto Sacchi [d,6] quinto.sacchi@dream-top.com

11 Francesca Verga [a,7] francesca.verga@polito.it

12

13 [a] Politecnico di Torino, Engineering Faculty, Department of Environment, Land and Infrastructure

14 Engineering, Torino, Italy

15 [b] TNO, Geological Survey of the Netherlands, Utrecht, the Netherlands

16 [c] Delft University of Technology, Department of Geoscience and Engineering, Delft, the Netherlands

17 [d] Dream s.r.l., Dedicated Reservoir Engineering and Management, Turin, Italy

18

19 **Abstract**

20 Stratigraphic forward modelling (SFM) provide the means to produce geologically coherent and

21 realistic models. In this paper, we demonstrate the possibility of matching lithological variability

22 simulated with a basin-scale advection-diffusion SFM to a data-rich real-world setting, i.e. the

23 Holocene Rhine-Meuse fluvio-deltaic system in the Netherlands. SFM model calibration to real-world

24 data in general has proven non-trivial. This study focuses on a novel inversion process constrained by

25 the top surface and the sand proportion observed at specific pseudo-wells in the study area. Goodness-

26 of-fit expressed by a new fitness function, gives the error calculated as the average of two calibration

27 constraints. Computational efficiency was increased significantly by implementing a new

28 optimization process in two hierarchical steps: a) optimization in terms of sediment load and

29 discharge, which are the most influential parameters having the largest uncertainty and b)

30 optimization with respect to the remaining uncertain parameters, these being sediment transport

31 parameters. The calibration process described allows for the most optimal combination of achieving

32 acceptable levels of goodness-of-fit, feasible runtimes and multiple (non-unique) solutions to obtain

33 synthetic stratigraphic output best matching real-world datasets.

34 By removing model realizations which are geologically unrealistic, calibrated SFM models provide a

35 multiscale stratigraphic framework for reconstructing static models of reservoirs which are consistent

36 with the palaeogeographic layout, basin-fill history and external drivers (e.g. sea level, sediment

37 supply). The static reservoir models that are matched with highest certainty therefore contain the

38 highest geological realism and may be used to improve deep subsurface reservoir or aquifer property

39 prediction.

40 The new methodology was applied to the well-established Holocene Rhine-Meuse dataset which

41 allows a rigorous testing of the optimization and the calibrated SFM allows investigation of controls

42 of the Holocene development on the sedimentary system.

43

44 **Keywords:** Stratigraphic forward modeling; basin modeling; fluvio-deltaic; inverse algorithm; model

45 calibration

46 **Nomenclature**

47 SFM: Stratigraphic forward modeling

48 sl: Sediment load

49 q: Discharge

50 e_s: Exponent of slope

51 c_s: Stream transport coefficient

52 NA: Neighborhood algorithm

53 n_s: Initial population

54 n_{dim}: Number of uncertain parameters

55   max_H: Maximum reservoir thickness

56   N: binary parameter

57   d.o.f.: degree of freedom

58

59   **1. Introduction**

60   Reservoirs with complex sedimentary heterogeneities such as low net-to-gross channelized deposits

61   hold significant amounts of energy resources worldwide. Despite locally good reservoir quality, the

62   estimation of reservoir properties in these heterogeneous deposits remains highly uncertain. The

63   inherent heterogeneities in these deposits necessitate geological reservoir models, which are typically

64   based on stochastic geometric and interpolation methods (Deutsch, 2002). Such methods generate

65   solutions which are locally optimal, capturing the overall setting but are not constrained by the large-

66   scale geological setting of the reservoir (Weltje et al., 2013) nor include processes associated with

67   sediment dispersal and deposition. Stratigraphic forward models (SFMs), that combine topographic

68   diffusion and advective transport equations, are well suited for investigating the morphodynamic and

69   resulting stratigraphic evolution of sediment dispersal systems over a wide range of spatial and

70   temporal scales (Granjeon and Joseph, 1999; Paola, 2000; Meijer, 2002; Hajek and Wolinsky, 2012).

71   Using SFM's inherent holistic approach and geological results, they provide attractive tools for

72   incorporating basin-scale information at the reservoir scale through the conditioning of geological

73   data in a variety of ways (Cross and Lessemger, 1999; Wijns et al., 2004; Imhof and Sharma, 2006;

74   Charvin et al., 2009; Falivene et al., 2014).

75   Efficiency in matching the data is essential because it determines the applicability of SFMs in real

76   field cases (Bertonello et al., 2013). Karssenberg et al. (2001, 2007) demonstrated the possibility of

77   conditioning SFMs to well data using a simple 3D alluvial architecture model characterized by a

78   single channel belt moving by avulsion over an aggrading floodplain. Sacchi et al. (2015, 2016)

79   implemented the method proposed by Weltje et al. (2013) for conditioning the stratigraphic output

80   derived from SimClast (Dalman and Weltje, 2008, 2012), a basin-scale advection-diffusion model of

81   fluvio-deltaic systems, in which the channels are represented by sub-grid elements. This SFM

82   provides a more efficient sediment transport algorithm for reproducing channelized flow as opposed

83   to conventional linear diffusion models (Meijer, 2002; Dalman and Weltje, 2008; Falivene et al.,

84   2014; Karamitopoulos et al., 2014; Sacchi et al., 2016).

85   This workflow has been shown to work in a synthetic setting. The simulated channel occurrences

86   were: a) fitted (conditioned) to synthetic seismic and local well data and b) integrated as soft

87   constraints in geostatistical reservoir modelling. The static reservoir models that were constrained to

88   maintain the quantitative coherence with the synthetic large-scale geological setting improved

89   predictive power relative to the models using local well data only.

90   In this case study, we conditioned SimClast (output/channel occurrences) to a data-rich real-world

91   setting, i.e. the Holocene Rhine-Meuse fluvio-deltaic system. The calibration dataset consists of

92   detailed lithological information obtained from GeoTOP, a high-resolution 3D voxel model that

93   captures the distribution of channel bodies and overbank fines of the fluvial-deltaic deposits in the

94   shallow subsurface down to 50 m below mean sea level (Stafleu et al., 2011; 2012; Van der Meulen et

95   al., 2013; Maljers et al., 2015: Stafleu and Dubelaar, 2016; Stafleu and Busschers 2017).

96   The applicability of a new workflow is demonstrated to a real-world setting through the

97   implementation of a hierarchical optimization approach. This approach significantly differs from the

98   one proposed by Sacchi et al. (2015, 2016), which adopted a less efficient Quasi-Monte Carlo

99   approach with systematic sampling to explore the SFM parameter space. In fact, matching the SFM

100 output to a real-world dataset requires a highly complex suite of parameters and calibration

101 constraints compared to synthetic datasets. Therefore, a more efficient matching routine was required

102 to minimize the number of runs to find the most optimal solution or solutions. Moreover, Sacchi et al.

103 (2015) used a well calibration fitness functions based on well tops and lithological logs which turned

104 out to be less effective for the inversion process. Therefore, in this study the well calibration function

105 is based on the average net-to-gross values at wells to manage the scale difference between well

106 (meter scale) and SFM (kilometer grid scale) information, which can be problematic when calibrating

107 well data (Sacchi et al., 2016), This is in line with Falivene et al (2014), who observed that the

108 representativeness problem could be mitigated by averaging over relatively large intervals.

109 By using the data-rich Holocene-Rhine Meuse GeoTOP model the robustness of the workflow is

110 illustrated and expanded where necessary. The predictive capabilities by incorporating synthetic

111 stratigraphy created by the SFM through the sedimentary processes are shown. Lessons learned may

112 be taken to future applications in deeper subsurface examples for accurate resource estimation. In

113 addition to testing hypotheses on the controlling parameters of the sedimentary system in question, the

114 matched/calibrated basin-scale model allows further use in constraining static models of channelized

115 reservoirs.

116

117

118

119 **2. Method**

120 The proposed methodology may be summarized as follows (Figure 1):

121 - Pre-processing

122   ✓ Characterization of the reference case: Holocene Rhine-Meuse fluvio-deltaic system

123   ✓ Definition of the constraints used for the calibration process

124   ✓ Sensitivity analysis to extrapolate the range of the input parameters used for SFM

125 - Inversion process for SFM calibration

126   ✓ Stratigraphic forward modeling using SimClast

127   ✓ Application of the Neighborhood Algorithm to explore the domain of the unknown

128   input parameters of SFM

129 - Result analysis

130   ✓ Comparison between the calibrated models from SimClast and the reference GeoTOP

131   model

132

133 Our approach builds on the workflow proposed by Sacchi et al. (2015, 2016), but improves the

134 methodology for both the definition of the fitness function expressing the calibration constraints and

135 in the algorithm which explores the parameter space for optimal model calibration. Each step is

136 described extensively in the following sections.

137

138

139
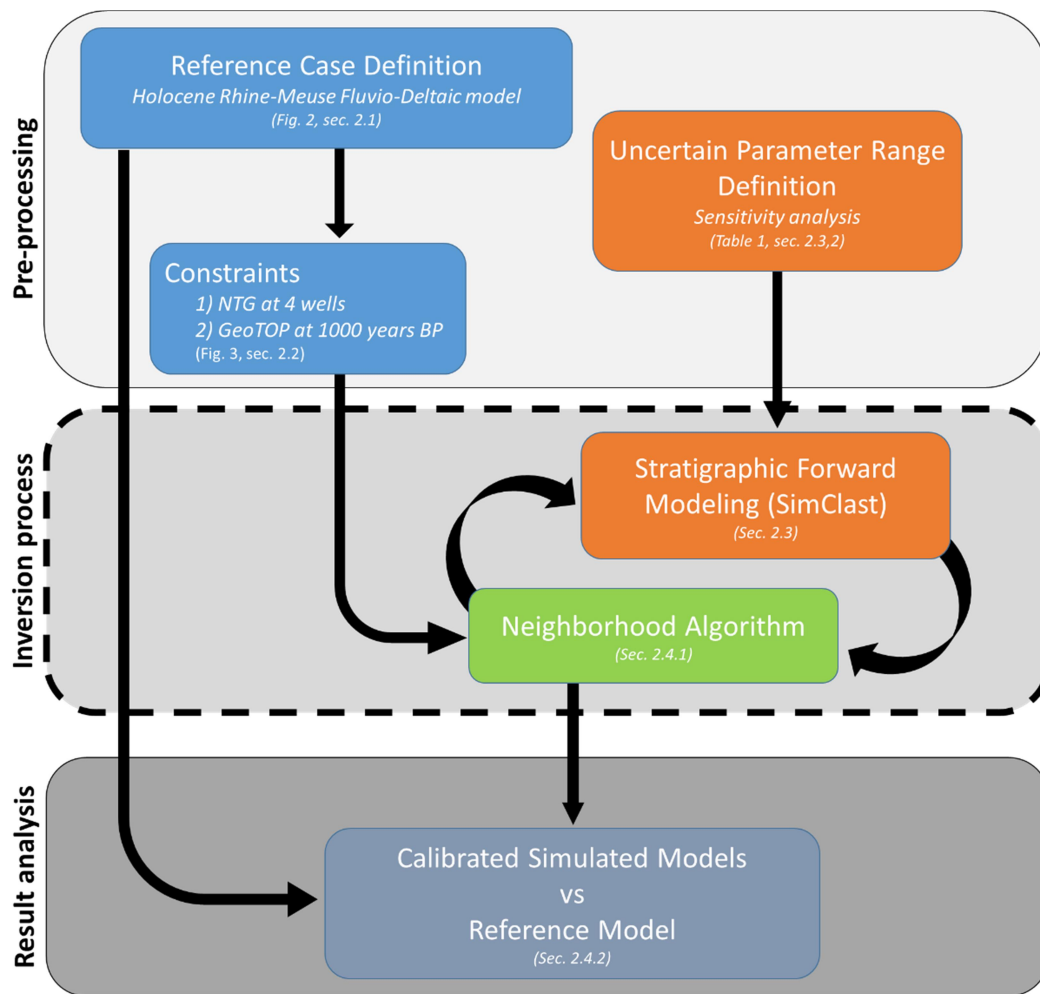
140 Figure 1: Stratigraphic Forward Model calibration workflow. The dashed box indicates the inversion
141 stage represented in fig. 6.

142

143

144

145 **2.1 Holocene Rhine-Meuse dataset**

146 TNO-Geological Survey of the Netherlands systematically produces detailed 3D geological models of

147 the Dutch subsurface (Van der Meulen et al., 2013). One of these models is the voxel model GeoTOP,

148 which describes the geometry of the shallow subsurface to a maximum depth of 50 m below mean sea

149 level (Stafleu et al., 2011; 2012; Van der Meulen et al., 2013; Maljers et al., 2015: Stafleu and

150 Dubelaar, 2016; Stafleu and Busschers 2017). The model is freely available online from the Survey's

151 web portal (www.dinoloket.nl/en). A major component of this static model are the Holocene Rhine-

152 Meuse fluvial deposits in the central part of the Netherlands (figure 2a). These fluvial sediments were

153 deposited during the Holocene sea level rise, which started in the western part of the area at ~9000

154 years BP, allowing base level rise and a complex of sand rich fluvial channel belt systems encased in

155 floodplain fines to be deposited. The channel belt positions in the GeoTOP model were taken from

156 the channel belt maps of Utrecht University (Berendsen and Stouthamer, 2001; Cohen and

157 Stouthamer, 2012). Base-level rise made that the tops of the younger channel belts occur at shallower

158 depths. Controlling parameters such as sea-level (Hijma and Cohen, 2010) and discharge/sediment

159 rates (Erkens et al., 2006; Koster et al., 2016) have been well studied and allow an estimate for the

160 boundary conditions to be made for the SFM.

161 This high-resolution 3D model has a grid discretization of 100 x 100 x 0.5 m and each voxel contains

162 subsurface information, including estimates of lithostratigraphy and lithology. The grid discretization

163 adopted, coupled with the very high borehole data coverage, allows GeoTOP to be used as a reference

164 scenario due to its accurate representation of the channel body geometries and associated spatial

165 lithological heterogeneity.

166 In the present study, the focus is on the, non-anthropogenically influenced, Holocene (9000-1000 BP)

167 fluvial deposits of the Zuid-Holland, Utrecht and Gelderland region, in the central part of the

168 Netherlands' subsurface. The 1000 year timeframe was chosen as younger deposits are influenced

169 heavily by anthropogenic dyke, dam construction and land reclamation. This region extends over

170 approximately 80 by 145 km and mainly consists of a complex fluvial channel system subdivided into

171 five distinctive Holocene channel belts deposits, each identified by a unique code number. The

172 channel belt complexes are classified from younger (shallower) to older (deeper): AEC, BEC, CEC,

173 DEC, EEC. (Figure 2a).

174

175 ***2.2 Definition of the calibration constraints***

176 Two calibration constraints were extracted from the GeoTOP model: (1) the top surface, analogous to

177 a 3D surface derived from seismic interpretation and time-depth conversion, covering the area

178 influenced only by fluvial and alluvial processes in the Rhine-Meuse delta; (2) the net-to-gross values

179 at four synthetic wells, arbitrarily located in order to uniformly investigate a hypothetical reservoir

180   area. The base surface was also used as an input constraint for the SFM simulation and it will be

181   described in paragraph 2.3.2.

182   The first calibration constraint was obtained by upscaling the GeoTOP model top surface,

183   corresponding to 1000 years BP (prior to anthropogenic influences), to a grid size of 1 x 1 km

184   conformable to the grid-resolution of the SFM grid size.

185   In order to obtain the net-to-gross at wells (the second calibration constraint) the GeoTOP model

186   (figure 2a) was indicator-coded into a channel-overbank depositional facies model (figure 2b). The

187   facies differentiation was performed by assigning a value of 1 net-to-gross to channel belt cells and 0

188   to overbank cells. Subsequently, net-to-gross data at four synthetic well locations was extracted from

189   the net-to-gross model (figure 3a and 3b).

190

191
192
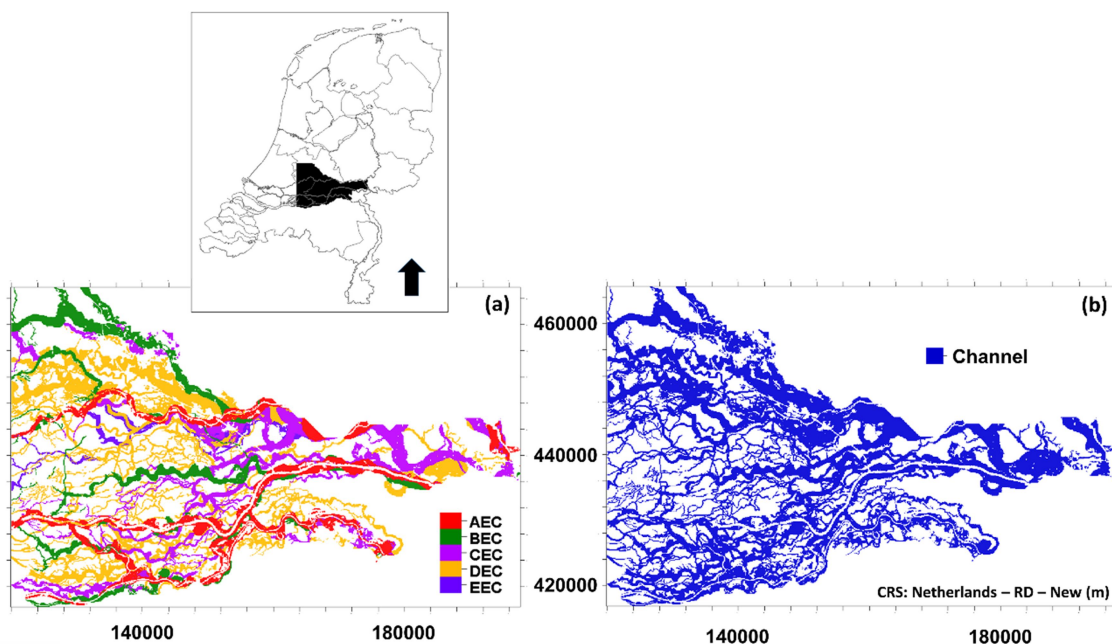
193   Figure 2: (a) Map view of the GeoTOP model with channel belt classification indicating relative ages

194   (from younger to older: AEC, BEC, CEC, DEC, EEC); the (b) indicator-coded depositional model

195   showing channel deposits only (Coordinate reference system: RD coordinates). In both models, the

196   overbank fines have been made transparent.

Figure 3: Calibration constraints. (a) Top surface (1000 years BP) of GeoTOP model with indication of the reservoir area and well locations (Coordinate reference system: Netherlands – RD – New); (b) depositional facies logs at the synthetic wells of the GeoTOP model (left column) and simplified indicator-coded depositional model which differentiates between channel and overbank facies (right column).

203

2.3 SFM description and setup

2.3.1 Model description

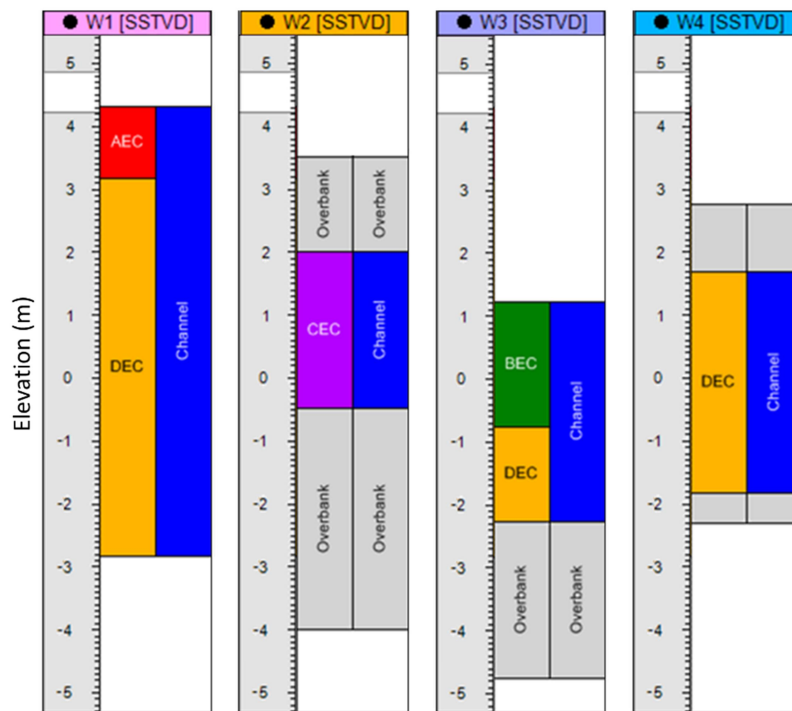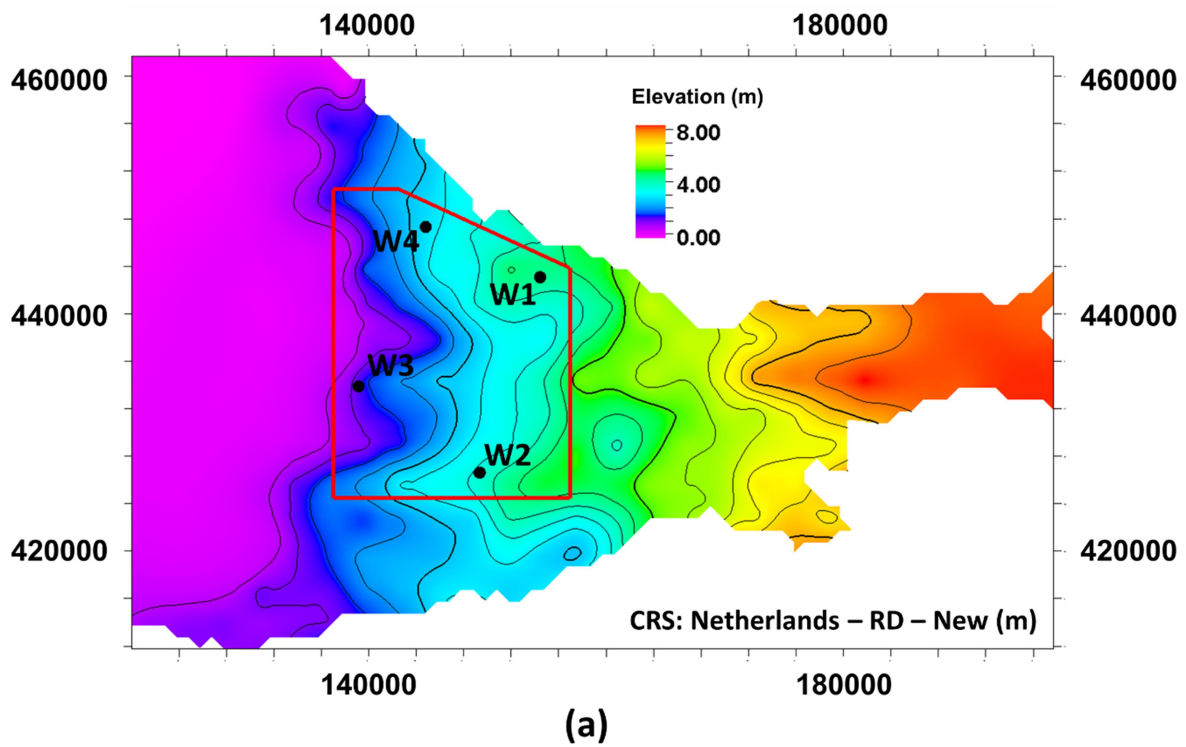A basin-scale model of river-shelf evolution (Meijer, 2002) combined with a sub-grid parameterization of fluvio-deltaic processes and stratigraphy (SimClast: Dalman and Weltje, 2008, 2012) was used to simulate the stratigraphy. While the grid size (1 by 1 km in this study) used for basin simulations does not allow the model to resolve sedimentary structures on the scale of individual channel belts, the implicit (subgrid) sedimentary processes included do allow a more realistic sedimentary architecture to develop as compared to diffusive basin scale models. Sedimentary processes relevant for this study are included by sub-grid parameterization of avulsions and mouthbar-induced bifurcations. Avulsions occur as a consequence of channel belt aggradation and superelevation whereas mouthbar-induced bifurcations dominate the terminal parts of the sediment dispersal system where delta lobes grow and topographic gradients are low or the system enters the marine domain. In order to adequately test the new optimization routine (see paragraph 2.4) and keep the parameter space within feasible dimensions the numerical experiments in this study did not include sedimentary processes associated with coastal and backwater dynamics (e.g. waves and tides). This model version adequately represents sedimentary processes shaping the stratigraphy, as the area of interest is influenced only by fluvial and alluvial processes in the Rhine-Meuse deposits during the Holocene.

2.3.2 Setup

The well studied Rhine-Meuse deposits allows a multitude of controlling parameters to be used. Incorporating all would result in a high dimensional parameter space, thereby resulting in an order of magnitude increase of number of computational runs. Therefore simplifications were made by assuming space differential subsidence, temporal variations in sediment supply and water discharge out of scope for this study.

From the available dataset, several input parameters were extracted to be used in SimClast. Simulation time was set to 8000 years (9000 to 1000 years BP) corresponding to the main

231   accumulation phase of sediment in the Holocene Rhine-Meuse delta (Erkens et al., 2006; Hijma et al.,

232   2009; Hijma et al., 2011). The initial topography, representing the top of the Rhine-Meuse fluvial

233   paleovalley systems and its flanks at the onset of Holocene relative sea-level at ~9000 years BP, was

234   taken from Koster et al. (2016) (figure 4). The surface represents an up-scaled version of a high-

235   resolution (100 by 100 m) grid that is used internally in the GeoTOP model workflow. The surface

236   extends over an area of 78 by 178 km and has a topographic elevation ranging from 13 to -27 m with

237   an average slope of about 0.01° dipping to the west. The grid discretization used is 1×1 km as this

238   scale is a good balance between data resolution and computer runtime. Two river inlet locations were

239   used, for the Rhine and Meuse river systems, and values of sediment supply (*sl*) and water discharge

240   (*q*) rate were assigned accordingly. The SimClast setup also required stream and diffusive transport

241   set coefficients, representing sediment transport efficiency. Both the environmental parameters (*sl* and

242   *q*) and the coefficients were investigated with preliminary sensitivity analyses meant to investigate the

243   impact of each single unknown separately. To this end, a preliminary uncertainty range was assigned

244   to the environmental parameters and the coefficients. The fixed ratio assumed between Meuse and

245   Rhine environmental parameters was also object of sensitivity.

246   Starting from a base case, obtained by choosing for each unknown the mid value of its uncertainty

247   range, SFM simulations were performed by varying only one unknown at a time, covering the

248   uncertainty range with a loose sampling interval. The relative influence of each unknown was

249   analyzed in terms of top surface elevation, average net-to-gross as well as channel layout. These

250   sensitivity analyses showed that the sediment load, discharge, exponent of slope and stream

251   coefficient had the most impact on the simulation results. These four parameters were assigned a

252   range to explore the associated uncertainty while the other parameters were assigned a fixed value. In

253   addition, from the results of the sensitivity analysis a ratio of 1/3 between Meuse and Rhine was

254   individuated. Table 1 shows the fixed values assumed and the ranges explored for the main

255   parameters of basin simulations used in the sensitivity analysis and in the subsequent stages. A

256   mismatch exists between the sediment load and discharge values from literature (section 2.1) and the

257   individuated used in SimClast. Therefore, the matching of SFM to real world results may show a

258   strong non-uniqueness for the various outcomes. Nonetheless, the main objective of our work focused

259　on the matching routine, therefore further study should be addressed in improving the SimClast

260　matching of the environmental parameters.

261

262　The river entry points were positioned along the eastern boundary of the initial surface and they were

263　assumed to be fixed in time, a feature that is reasonable based on geological observations (Stouthamer

264　et al., 2011). The sediment-supply consists of two discrete classes: sand and clay. Both the sediment

265　entry locations and the sediment and water rates were time invariant for each simulation. The

266　variation of the sea level was defined through the relative sea-level curve from Hijma and Cohen

267　(2010) which describes the groundwater change over the considered simulation time.
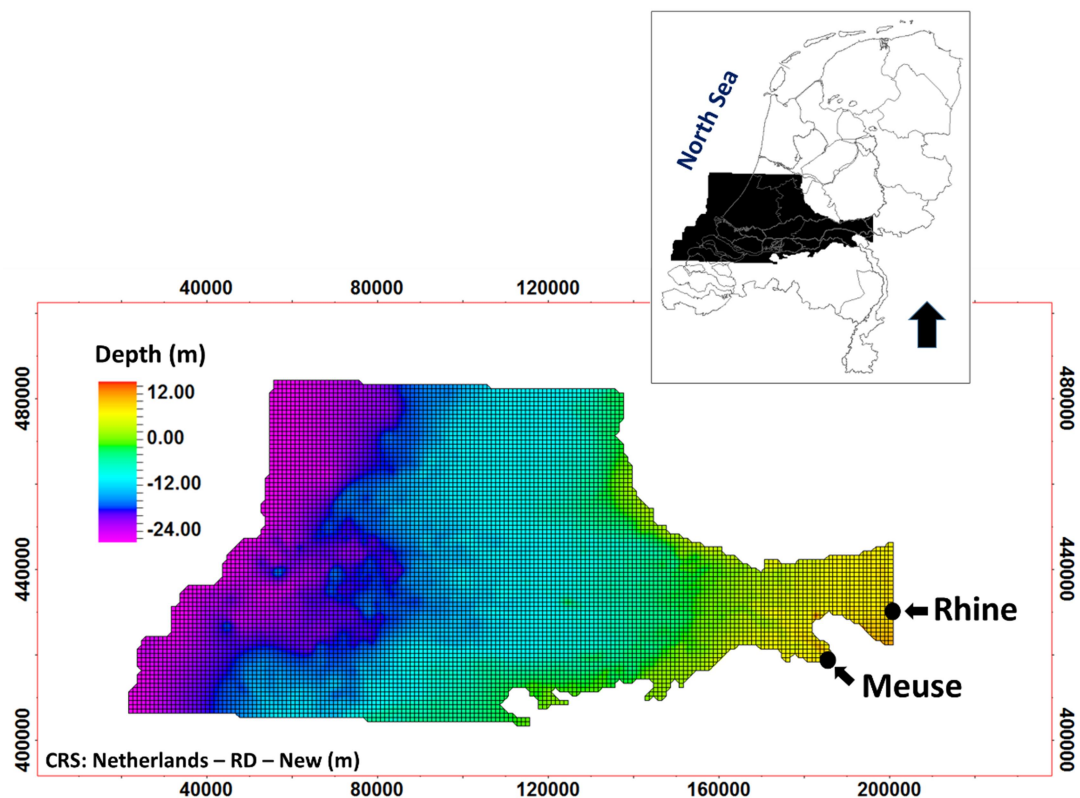
268

269

270　Figure 4: Model base surface (9000 years BP; Koster et al., 2016) used for basin simulations. The

271　river inflow locations are indicated on the eastern boundary of the surface.

272

273　Table 1: Values and ranges of the main input parameters used for basin simulation.

274

Rhine sediment load (kg/s)	sl	70-120
Rhine discharge (m^3/s)	q	100 - 1500
Exponent of slope [-]	e_s	1 - 5
Stream coefficient [-]	c_s	0.1 - 8
Exponent of discharge [-]	e_d	1
Transport length deposition/erosion [-]	tl	1500
Threshold discharge [m/yr]	t_d	12.5

275

276

277

278

279

280 ***2.4 Matching routine***

281 *2.4.1 Neighborhood Algorithm*

282 A variation of the direct-search gradient-free Neighborhood Algorithm (NA) (Sambridge 1999, 2001,

283 Imhof and Sharma, 2006, 2007) was used to calibrate the SFM. This iterative sampling algorithm is

284 applicable to a wide range of inversion problems, particularly those where the relationship between

285 the observations and the unknowns (a finite number of model parameters) is complex and non-linear

286 (e.g. Imhof and Sharma, 2006; Sambridge, 2001).

287 At the initial stage, the implemented algorithm generates n_S sets of uncertain model parameters by

288 randomly sampling each parameter inside a user-specified range following a uniform distribution

289 (table 1) and the corresponding stratigraphic models are simulated. The magnitude of the initial

290 population (n_S) is generally set based on the number of searching dimensions (i.e. number of uncertain

291 parameters, n). We set $n_S = n^{3.5}$, according to the empirical saturation value from Sambridge (2001),

292 i.e. the minimum value of samples allowing the NA to perform well. Successively, for each sampled

293 model output, the associated fitness is evaluated, based on the calibration constraints described in

294 section 2.4.2. In optimization terminology, the initial set of sampled models is called initial

295 population; the parameter space is a multidimensional domain delimited by the range of values for

296 each uncertain parameter, where each parameter represents a searching dimension.

297 At each iteration, the entire parameter space is partitioned into a set of n-dimensional Voronoi cells,

298 where n is the number of uncertain parameters characterizing the model. Each cell delimits the nearest

299 neighbor region of an element of the current population, which is the cell centroid. Voronoi cells are

300 ranked according to the corresponding fitness, which is assumed to be constant within the cell and

301 equal to the fitness of the cell centroid (Sambridge 1999a). New parameter sets are sampled from both

302 low fitness cells and random ones; this allows the algorithm to shift the search to new areas of the

303 parameter space once low-error-model regions have been oversampled (i.e. local minima). This is a

304 strong point of the technique because it allows non-unique outcomes. For each of the selected

305 Voronoi cells new samples are generated by uniform random walk within the cell (Sambridge, 1999a,

306 1999b).

307 The new samples generated at each iteration are added to the population; the corresponding

308 stratigraphic models and fitness functions are calculated. As more models are added and evaluated,

309 the NA focusses on low-error areas of parameter space and densely sample these. The inversion

310 algorithm is run for several iterations until a stop criterion (a maximum number of iterations reached

311 or stagnation in the fitness function) is met.

312 The outcome of the inversion is an ensemble of diversified calibrated models rather than the lowest

313 error model.

314 The methodology is not well suited for high number of uncertain parameters because the

315 neighborhood search via the Voronoi approach loses efficiency; in fact, a high dimensionality results

316 in the data space being sparsely populated with data points. However, the NA has several advantages:

317 • it is a good compromise between exploration and exploitation

318 • it can manage multimodal functions (i.e. escape from local minima)

319 • it can obtain a plurality of calibrated models instead of a single best fit

320 • it considers all the previously attempted parameter combinations to produce new candidate

321 solutions

322 • it allows for straightforward parallelization

323

324

325 *2.4.2 Fitness function*

326 The outcome of SimClast simulations conducted for each sampled set of uncertain parameters is

327 compared with the GeoTOP constraints. Two calibration constraints are considered (section 2.2): (1)

328 the 1000 years BP top surface analogous to a seismic 2D surface information covering the area

329 influenced only by fluvial and alluvial processes in the Rhine-Meuse delta; (2) the net-to-gross data at

330 four synthetic wells, extracted from the GeoTOP model, located within a hypothetical reservoir area.

331 The cumulative goodness of fit is quantified by the total misfit with respect to these constraints,

332 expressed by:

333

334
$$Error = \frac{RMSE_{surface} + RMSE_{wells}}{2} \tag{1}$$

335

336 where $RMSE_{surface}$ is the root mean square error between the elevation of GeoTOP top

337 surface ($Z_{GeoTOPi}$) and the corresponding surface obtained by the stratigraphic forward model

338 described in paragraph 2.3 (Z_{SFMi}); the quote difference was normalized with respect to the maximum

339 reservoir thickness ($max_H = 8$ m):

340
$$RMSE_{surface} = \frac{\sqrt{\sum_{i=1}^{n_{points}} \left(\frac{Z_{GeoTOPi} - Z_{SFMi}}{max_H} \right)^2}}{n_{points}} \tag{2}$$

341

342 where n_{points} is the number of grid points discretizing the surface.

343 The normalizations applied make the contribution of such calibration constraints comparable with the

344 well calibration and allowed to summarize them into a single fitness function.

345 Eq. 2 slightly differs from the fitness function based on top surfaces presented in Sacchi et al. 2014;

346 no tolerance was considered here due to the relatively thin layer of sediment in the case study.

347 The root mean square error relative to well calibration reads:

348

349
$$RMSE_{wells} = \frac{\sqrt{\sum_{i=1}^{n_{wells}} (N_{GeoTOP_i} - N_{SFM\,i})^2}}{n_{wells}} \tag{3}$$

350

351 where N is a binary parameter arising from the comparison of the average net-to-gross value at

352 calibration wells ($\overline{NTG}$) with a threshold value ($\alpha = 0.3$):

$$N = \begin{cases} 1 \ if \ \overline{NTG} \geq \alpha \\ 0 \ if \ \overline{NTG} < \alpha \end{cases} \qquad (4)$$

N_{GeoTOP_i} is calculated by averaging the arithmetic mean of the net-to-gross values at each calibration well (i) in the GeoTOP dataset ($\overline{NTG_{GeoTOP_i}}$), while $N_{SFM\ i}$ is calculated by averaging the net-to-gross value at each calibration well (i) in the modeled stratigraphy ($\overline{NTG_{SFM\ i}}$).

The above fitness functions (eq. 3) differ from the well calibration fitness functions proposed by Sacchi et al., 2015, which were based on well tops and lithological logs. To manage the scale difference between representativeness of the well (meter scale) and SFM (kilometer grid scale) information the comparison at the wells is made here in terms of N (eq.4) instead of lithological log or net-to-gross. In fact, Falivene et al (2014) observed that the representativeness problem could be mitigated by averaging over relatively large intervals. However, in the presented case the reservoir thickness is quite thin (8m in the thickest part) and the averaging was not sufficient to account for the uncertainty associated with well calibration data and the simplifications inherent to the SFMs, thus a threshold was introduced on the averaged values.

Figure 5 shows the application of the threshold to the net-to-gross map of the GeoTOP model in which only the cells containing net-to-gross above the threshold are considered channels.
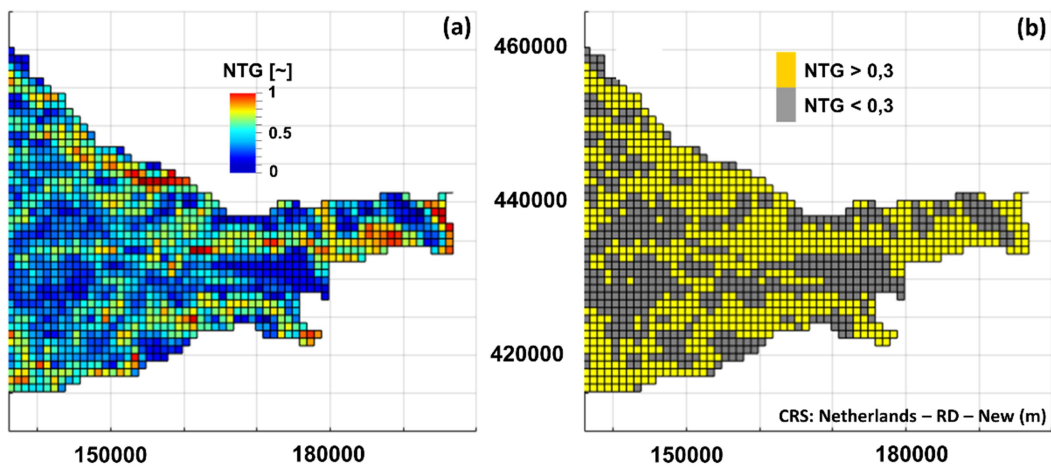
373   Figure 5: (a) Net-to-gross map derived from GeoTOP by upscaling the 100 m cells in Figure 2b to the

374   1 km cells of the model; (b) corresponding map with the threshold applied (Coordinate reference

375   system: Netherlands – RD – New).

376

377   *2.4.3 Two-stage optimization approach*

378   The optimization process was performed over two hierarchical steps through the implementation of

379   the NA. Preliminary sensitivity analyses (see section 2.3.2) were performed in order to identify the

380   model parameters with the greatest influence on the outcome. Sediment load (sl) and discharge (q)

381   turned out to dominate the SFM response in terms of fitness function value and visual inspection of

382   the channel layout. Two other parameters showed a minor but significant impact on sediment

383   transport efficiency in SimClast: the exponent of slope (e_s) and the stream transport coefficient (c_s) .

384   This suggested the adoption of a 2-stage optimization approach: the problem is decomposed by first

385   optimizing over a subset of the uncertain parameters that most significantly influence the model

386   realization and then optimizing over the remaining significant uncertain parameters, thus reducing

387   complexity:

388

389   •   Step 1: optimization with respect to the uncertain parameters with highest impact on level of

390   fitness (sl and q)

391   •   Step 2: optimization with respect to the remaining uncertain parameters (e_s and c_s), in this step

392   sl and q values from the previous step are assumed constant

393

394   This approach allows us to mitigate the main disadvantage of NA, i.e. the loss of performance related

395   to the gradually increasing size of parameters space.

396   The comparison between the 1-stage and 2-stage approaches is illustrated in figure 6.

397   In order to locate multiple acceptable regions in parameter space and thereby addressing the inherent

398   non-uniqueness in geological synthetic models; Step 2 was run for a number of different promising sl

399   and q combinations identified in Step 1. In order to identify clusters of potentially valid parameters

400   combinations from the final population of Step 1, along with the best sampled solution, two other

401   samples were selected based on a trade-off between the corresponding error and the parameter

402   diversity from the best solution. This selection process was manually done by visual inspection of the

403   Voronoi diagram of the fitness map (fig. 7); automation of the selection of promising parameters sets

404   will be part of future developments.

405   The proposed 2-stage NA approach with 4 parameters optimized sequentially in groups of 2 (i.e. 2

406   parameters optimized at each step) was compared with the 1-stage NA approach, with four parameters

407   optimized simultaneously. In both cases, the explorative feature of the algorithm was emphasized by

408   spreading the samples over several NA cells: at each iteration, new models in number equal to half of

409   the initial population were generated, each extracted from a different Voronoi cell. In order to avoid

410   trapping in local minima, 1/4 of the resampled cells were chosen from the fitness ranking, while 3/4

411   were chosen randomly from the remaining cells. The above relationships were calibrated against

412   analytical multidimensional multimodal test functions: Styblinski–Tang function (Styblinski and

413   Tang, 1990), Rosenbrock function (Rosenbrock, 1960), Holder table (Mishra, 2006), Bukin function

414   n°6 (Bukin, 1997) in a preliminary validation phase.
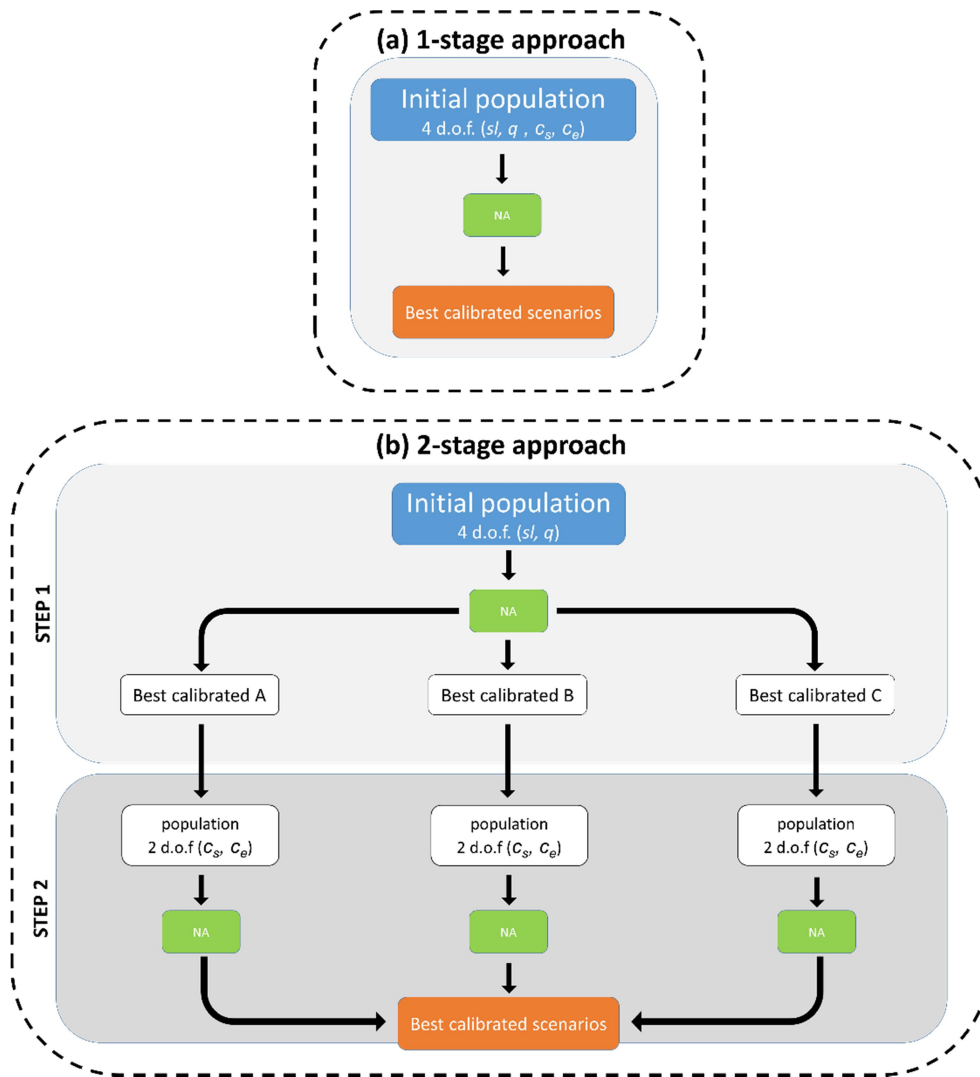
415

416

417

418
419
420   Figure 6: Comparison between the flowchart of (a) 1-stage with 4 degrees of freedom (d.o.f.) and (b)
421   2-stage optimization approach with 2 degrees of freedom. The dashed boxes refer to the inversion
422   process box in figure 1.
423
424
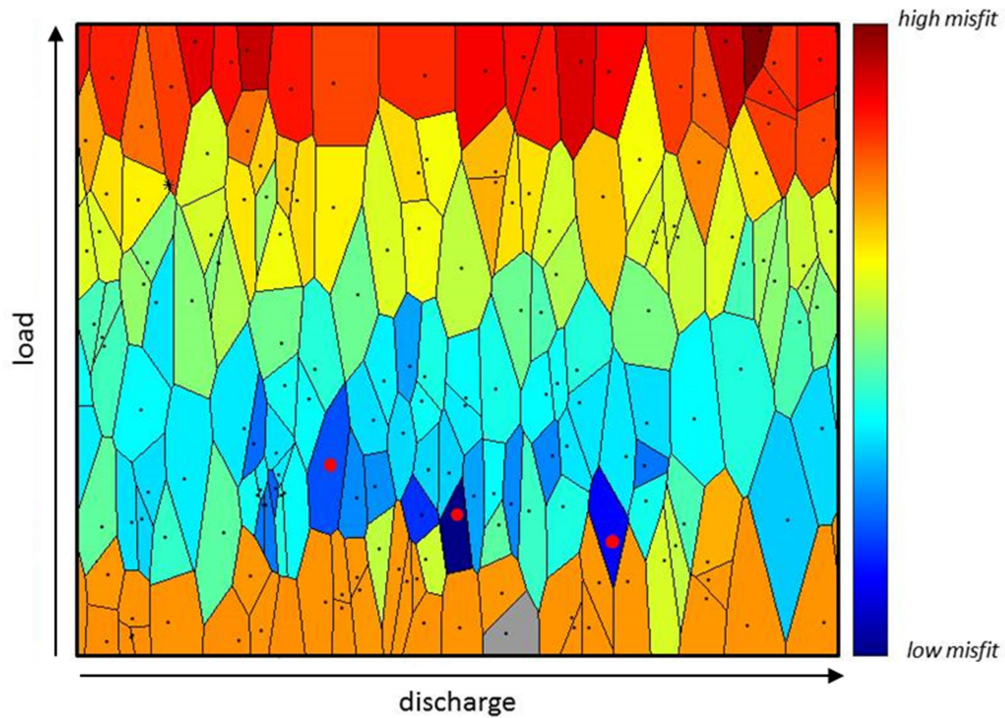
Figure 7: Example of qualitative Voronoi map with identification of local minima (red dots). A fixed ratio between the Meuse and Rhine values is assumed. The forward model appears to be more sensitive to the sediment load but the water discharge has a significant impact as well.

3. Results

The first part of the work concentrated on the comparative analysis of the proposed 2-stage NA approach with respect to the 1-stage NA approach, (paragraph 2.4.3) evaluating their capability to sample a range of valid models that are consistent with typical calibration constraints. The optimization results were compared in terms of evolution of the fitness function with the number of models sampled during the iterative process. The error evolution is obtained by selecting the error at each iteration corresponding to the element of the current population exhibiting the best fitness, and

441   plotting it against the population cardinality (i.e. number of sampled models). Figure 8 illustrates an

442   example of the evolution of fitness function (gray line) compared with the evolution of each

443   calibration constraint (well calibration, green line, and top surface calibration, orange line) for the first

444   step of 2-stage NA approach. The fitness function (grey line) consistently decreases as the population

445   grows with iterations, while the evolution of each calibration constraint is not necessarily consistently

446   decreasing (e.g. orange line) because one of the two calibration constraints can decrease in fitness if it

447   is compensated by a significant improvement of the other calibration constraint.
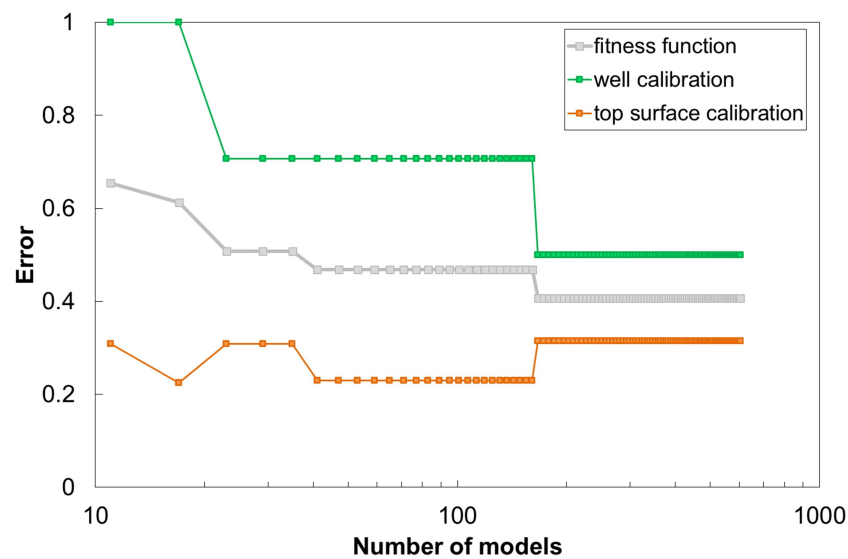

448

449   Figure 8: Evolution of the fitness function (gray line) compared with the evolution of each calibration

450   constraint (well calibration, green line, and top surface calibration, orange line) for the first step of the

451   2-stage NA approach; squares represent the iterations.

452   Figure 9 shows the comparison between the error convergence curves produced by the two

453   optimization approaches. The 1-stage approach is represented by a unique blue dotted line. The 2-

454   stage approach, instead, shows a branch from the first step, characterized by a single red line, to the

455   second step, characterized by three different lines (yellow, orange and brown) associated with the

456   three sets of fixed environmental parameters (sediment load and discharge), named Case A, Case B

457   and Case C respectively, selected among the final population of Step 1 based on the trade-off between

458   error value and parameter diversity from the best solutions (section 2.4.3). Notice that Case A shows

459   continuity of the error convergence curve between Step 1 and Step 2 because this scenario starts from

460   the set of parameters that exhibits the lowest error among the population of Step 1. Conversely, for

461   Case B and Case C a discontinuity is observed on the error convergence curve between Step 1 and

462   Step 2 because these scenarios start from two different sets of parameters explored in Step 1, which

463   are promising (i.e. higher error than the best solution of step1) but characterized by a higher error with

464   respect to the best solution of Step 1.

465   As described in paragraph 2.4.3, the initial number of the sampled models (i.e. initial population) is

466   calculated as a function of the parameters that are used in the inversion algorithm (i.e. number of

467   searching dimensions) and this explains why this number is much higher in the 1-stage (100)

468   compared to the 2-stage approach (11). The cardinality of the initial population, in turn, affects the

469   initial error value, which corresponds to the fitness of the best sample among the initial population. As

470   more models are added and evaluated through the iterations, all the curves converge towards low error

471   areas of the parameter space.

472   Table 2 shows the set of environmental parameters and coefficients used to simulate both the 1-stage

473   and the 2-stage scenarios.

474   Table 3 shows the average net-to-gross values at each well location for the 1-stage and 2-stage

475   approaches while table 4 shows the average top surface misfit for the 1-stage and 2-stage approaches.

476   The top surface misfit is obtained by calculating the differences in altitude at each grid surface map

477   location along the vertical direction. The results show that the 2-stage Case C scenario has the lowest

478   average net-to-gross misfit with respect the reference GeoTOP while the average surface misfit is

479   comparable in all the cases. The matching of the wells seems to have a random behavior, in fact we

480   did not observe a systematic problem in matching specific wells. As a way of example the top surface

481   misfit maps for the 1-stage and 2-stage scenarios are shown in figure 10.

482   Figure 11 shows net-to-gross maps of the reference case as well as of the simulated scenarios for both

483   the 1 and 2-stage approaches (Case A-B-C). All simulated maps show realistic representation of

484   convergent and divergent fluvial channel patterns typical of a distributary network.
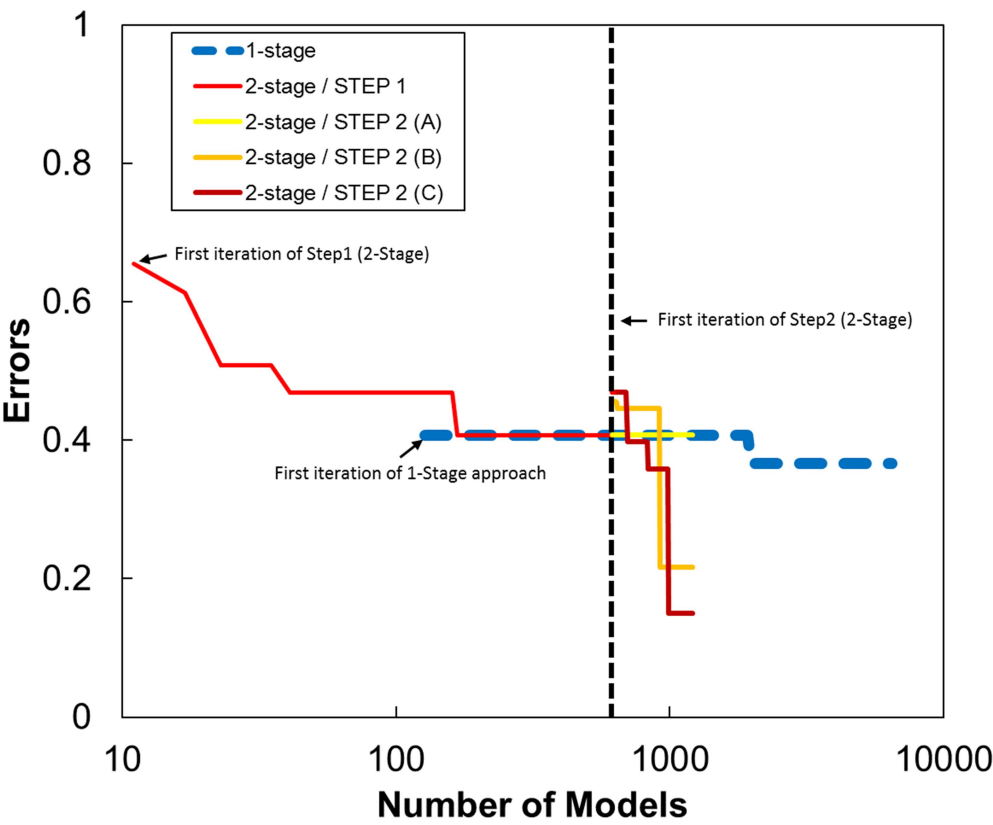
485

486

487   Table 2: Set of optimal environmental parameters and coefficients obtained from the 1-stage and the

488   2-stage scenarios.

489

	1-stage	2-stage (Step 1)	2-stage (A)	2-stage (B)	2-stage (C)
Rhine sediment load (*kg/s*)	58	54	54	49	66
Rhine discharge (m³/s)	1110	689	689	774	327
Exponent of slope [-]	3.85	2.38	1.95	2.64	3.92
Stream coefficient [-]	5.84	5.78	1.54	2.66	7.51

490

491

492

493

494 Figure 9: Comparison between the error convergence curves produced by the 1-stage approach (blue)

495 and the 2-stage approach which is composed by a first step (red) and a second step, characterized by

496 three different lines (yellow, orange and brown) associated to the 3D set of fixed environmental

497 parameters (sediment load and discharge).

498

499 Table 3: Average net-to-gross at wells for the 1-stage and 2-stage approaches

500

	Well 1	Well 2	Well 3	Well4
GeoTOP	0.5	0.42	0.51	0.5
1-stage	0.38	0.36	0.39	0.41

2-stage_Case a	0.48	0.38	0.39	0.4
2-stage_Case b	0.38	0.39	0.37	0.43
2-stage_Case c	0.48	0.44	0.43	0.46

501

502   Table 4: Average top surface misfit for the 1-stage and 2-stage approaches with respect to GeoTOP

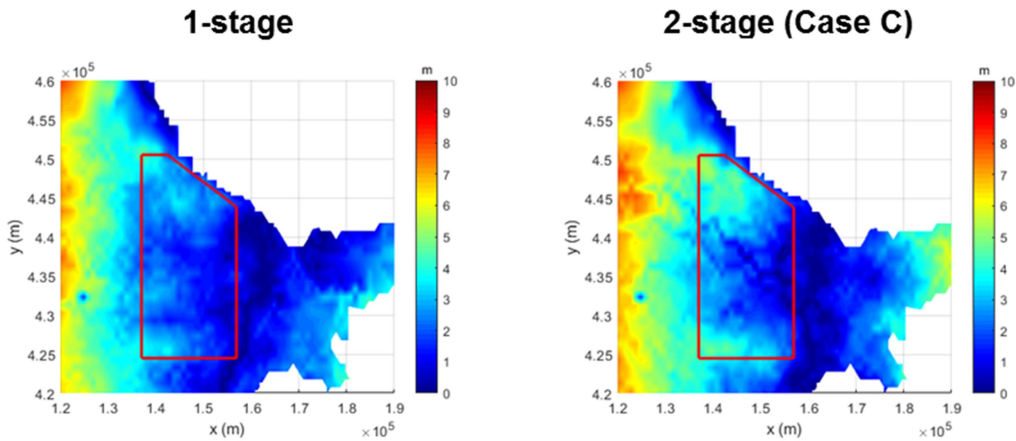|	Average Misfit (m)
1-Stage	2.96
2-stage_Case a	3.02
2-stage_Case b	3.6
2-stage_Case c	3.2

503

504

505   Figure 10: Surface misfit for the 1-stage (left) and the 2-stage Case C scenarios. The misfit map is

506   obtained by vertically subtracting the altitude at each grid location. The red polygon indicates the

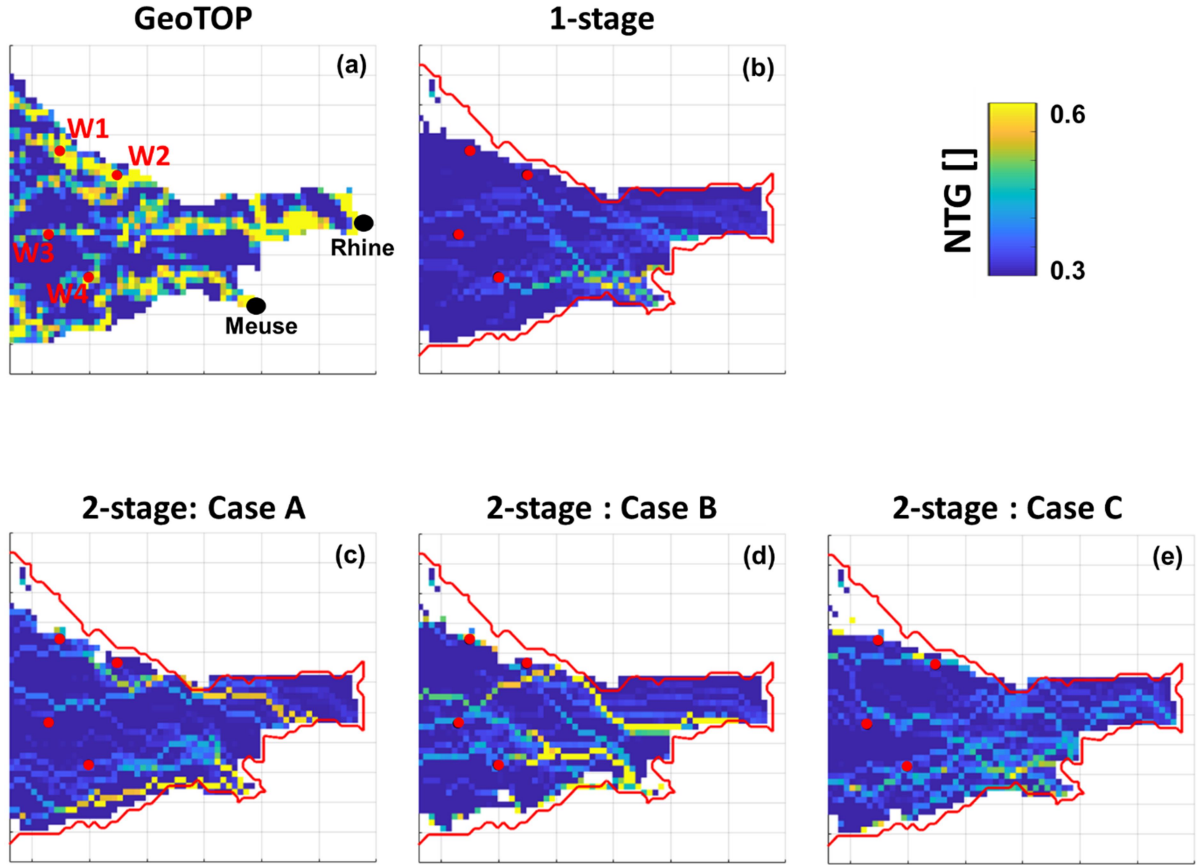507   hypothetical reservoir area.

508

Figure 11: (a) Upscaled GeoTOP net-to-gross map (1 km grid); (b) simulated net-to-gross map using the 1-stage approach; (c) (d) (e) three best net-to-gross map scenario obtained using the 2-stage approach (from left to right Case A, Case B and Case C). The color scale ranges between 0.3 and 0.6 net-to-gross in order to highlight the channel belts geometries. The well locations are indicated with red dots while the contour line of the GeoTOP top surface is indicated with the red line.

3.1 Stratigraphic expression of calibrated simulations

The SFM records very high resolution vertical stratigraphic intervals (averaged over grid cells of ~1 mm thickness). In order to compare with the GeoTOP data this stratigraphy is upscaled. Figure 12 shows both the actual synthetic stratigraphy with net-to-gross property of one example gridcell after a typical simulation and the upscaled net-to-gross. Although upscaled net-to-gross property is used to compare with the GeoTOP model at well locations, actual high resolution net-to-gross stratigraphic

523   expression output by the SFM may still be used for other purposes such as detailed constraining of

524   reservoir models.
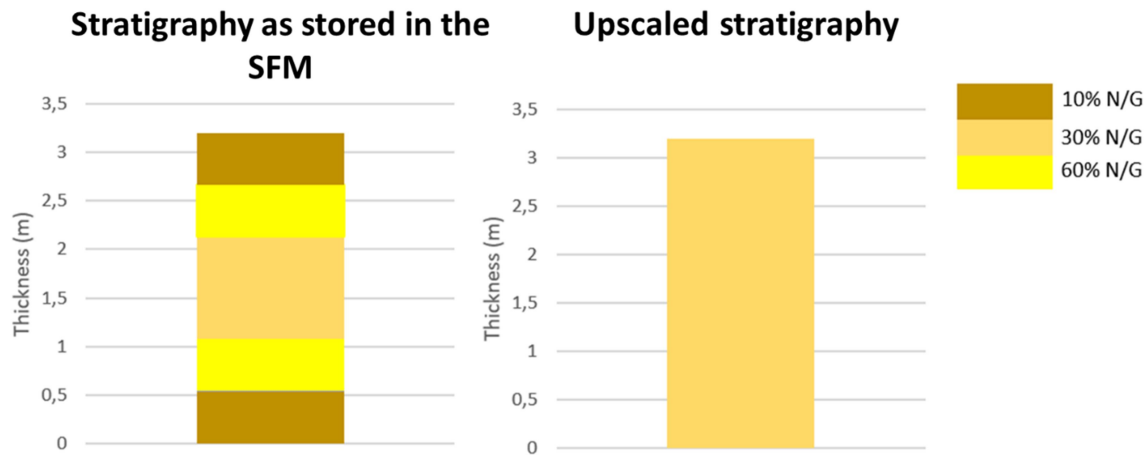
Figure 12: Example of synthetic stratigraphy in one gridcell generated by the SFM (left) showing the low net-to-gross units at base and top, sandy units in yellow and mixed units in orange. Upscaled stratigraphy as extracted from the high resolution stratigraphy (right).

531   The stratigraphic output of the SFM is highly variable. The misfit of the 1-stage example run and the

532   best 2-stage run (Case C) is shown in map view in figure 10. This shows that there is a significant

533   variability in realizations after calibration of further parameter sets.

4. Discussion and conclusions

4.1 Matching optimization

The results outlined above show the possibility of matching lithological variations simulated with a basin-scale SFM to real data. In this numerical framework, accurate estimation of the SFM input parameters, especially initial topography and sediment entry points, ensured a reliable prediction of the spatial distribution of channelized deposits (Sacchi et al., 2015).

543　The results demonstrate that a significant improvement is obtained by implementing the novel two-

544　step optimization approach as compared to the approach using four variables simultaneously. In fact,

545　with the same number of sampled models the error is significantly lower (Case B and C) or nearly

546　equal (Case A) to the one produced by the 1-stage approach; moreover the 1-stage approach did not

547　succeed in obtaining results comparable with Case B or C even with a significantly larger number of

548　samples. This demonstrates that a hierarchical exploration of the variable space can be very efficient.

549　A small variation in one of the two leading parameters can have a greater impact on the fitness

550　function value than a variation of one of the two other parameters, thus masking possible progress due

551　to explorations in the remaining directions. On the other side the search space of each optimization

552　step of the 2-stage approach is much reduced with respect to the 1-stage, thus allowing better

553　exploration. The choice of using multiple starting points for the second step of the 2-stage approach

554　proved to be valuable to escape from the local minimum at the end of Step 1. In fact, Case A, which

555　uses the optimum arising from Step 1 to fix values of sediment load and discharge is trapped in the

556　local minimum while Case B and C are able to further improve the sampling.

557

558　*4.2 The stratigraphic variability in model output*

559　The outcome of the inversion process is an ensemble of diversified calibrated models, which

560　inherently capture a range of uncertainty. The uncertainty range largely depends on the amount and

561　type of data available as calibration constraints (i.e. well logs, well tops, seismic data). As illustrated

562　in figure 10 the difference in output of the model runs shows the strong non-uniqueness of the fluvial

563　sedimentary architecture despite only varying two parameters. This gives rise to the idea that the

564　diversified calibrated models may be combined to construct a set of probability density cubes of likely

565　net-to-gross occurrence to be used as a soft conditioning, as proposed by Sacchi et al. (2016), for

566　constraining reservoir scale models. Moreover, a Monte Carlo style post processing routine perturbing

567　the calibrated models outcome may be added to account for the natural variability inherent in the

568　sedimentary record which a deterministic SFM cannot capture. The interpretation of ancient deposits

569　is many faceted, this is shown by the mismatch between the best fit sediment loads and discharge

570　values in the model results (table 2) with the reference case (Figure 10). The outcome of our work in

571   matching SFM to real world results may show a strong non-uniqueness for the various outcomes.

572   However, the focus of this study is on optimizing the matching routine. Further optimization to match

573   the N/G maps (see Figure 10) and expanding on this subject is proposed for further study.

574

575   *4.3 Geological constraints*

576   Wave reworking enhances large-scale depositional connectivity by producing laterally extensive

577   sandy plains and beach-ridge complexes (Reynolds, 1999; Hampson, 2000). Similarly, tidal currents

578   tend to increase depositional connectivity by forming elongated sand bodies perpendicular to the

579   shoreline. However, the net effect of tidal activity becomes difficult to predict because it regulates

580   local accumulation of fine-grained sediments, which may affect the morphodynamic evolution of the

581   entire delta (Edmonds and Slingerland, 2010). These coastal processes will have a direct influence on

582   upstream fluvial processes in the modelled area by effectively changing the baselevel and sediment

583   transport capacities of the channels in question.

584   The mixing of sand with clay, peat formation and post-depositional processes (i.e. differential

585   subsidence) complicate further predictions of incision and sedimentation patterns in tidally influenced

586   distributary channels. Despite these potential problems, groundwater regime in the studied part of the

587   Holocene Rhine-Meuse was river-dominated (Koster et al., 2016). Thus, based on sedimentological

588   evidence it is not unreasonable to assume that our modelling approximations represented the

589   sedimentary evolution in the study area fairly well as the area in question was influenced to a lesser

590   extent by major peat deposition or tidal influence but was purely fluvial at time of deposition. Peat

591   deposition has been shown to stabilize the channel belts further, decreasing lateral migration and

592   increase the rate of filling by peat growth.

593

594   *4.4 Future work*

595   The workflow proposed in this study may be applied to deep, data sparse, reservoir or aquifers in

596   order to populate static geological models with sedimentary properties derived from the calibrated

597   SFM output. An additional use of SFM matched to real world data sets is by allowing conceptual

598   theories to be tested and quantified. i.e. the current model may be used to test models of avulsion

599   frequency in the Holocene Rhine Meuse fluvial system (Stouthamer et al 2011).

600   The challenge of predicting reservoir-quality distribution in channelized reservoirs requires detailed

601   knowledge about sediment-body geometry and heterogeneity at different scales (Martinius et al.,

602   2014). From this viewpoint, large-scale depositional connectivity which may be captured using the

603   basin-scale SFM needs to be complemented by quantifiable information about the 3D geometry of

604   architectural elements (i.e. channels, point bars, levees and crevasse splays) and their degree of

605   amalgamation (sensu Peter et al., 2017). In addition, the spatial distribution of geological properties

606   (e.g. petrophysical) need to be well described in order to more accurately predict reservoir-quality

607   distribution. In that respect, future developments should focus on integrating post-depositional

608   processes in SFMs, and in particular differential subsidence, tectonic control and early diagenetic

609   alterations by means of reactive transport modelling. Further study should also focus on the automatic

610   identification of the number of potential local minima that can be retained in the first stage of the

611   optimization procedure (Step 1). A possible approach could be to use a density-based clustering

612   algorithm, such as DBSCAN or OPTICS (Ester et. al, 1996; Ankerst et al., 1999) on a subsample of

613   the sampled population obtained by applying cut-off values to the objective functions based on the top

614   surface calibration (eq. 2) and well calibration (eq. 3) or to the combined error function (eq. 1).

615

616

617   **Computer code availability**

618   The related code is written in MATLAB 2018. The file name of related code is "NA_Basin". To

619   access the source file of the code, one can visit the repository on GitHub (https://github.com/REDD-

620   PoliTO/Optimization).

621

625

626   **References**

627   Ankerst, M., Breunig, M. M., Kriegel, H. P., & Sander, J. (1999). OPTICS: ordering points to identify

628   the clustering structure. ACM Sigmod record, 28(2), 49-60.

629

630   Berendsen, H.J.A. and E. Stouthamer 2001, Palaeogeographic development of the Rhine-Meuse delta,

631   the Netherland, Assen (Van Gorcum)

632

633   Bertonello, A., Sun, T., Li, H., Mariethoz, G. and Caers, J. (2013) Conditioning Surface-Based

634   geological Models to Well and Thickness data. Mathematical geosciences, 45(7), 873-893. DOI:

635   10.1007/s11004-013-9455-4

636

637   Bukin, A.D. (1997). New Minimization Strategy For Non-Smooth Functions, Budker Institute of

638   Nuclear Physics preprint BUDKER-INP-1997-79, Novosibirsk.

639

640   Charvin, K., Gallagher, K.L., Hampson, G. and Labourdette, R. (2009). A Bayesian approach to

641   inverse modelling of stratigraphy, part I: method. Basin Research, 21, 5–25.

642

643   Cohen, K.M., Stouthamer, E., 2012. Digitaal Basisbestand Paleogeografie van de Rijn-Maas Delta.

644   DANS. https://doi.org/10.17026/dans-x7g-sjtw.

645

646   Cross, T. and Lessenger, M. (1999). Construction and application of stratigraphic inverse model. In:

647   Harbaugh, J.W. et al. (eds.), Numerical Experiments in Stratigraphy: Recent Advances in

648   Stratigraphic and Sedimentologic Computer Simulations. SEPM Special Publication 62, 69-83.

649

650   Dalman, R.A.F. and Weltje, G.J. (2008). Sub-grid parameterisation of fluvio-deltaic processes and

651   architecture in a basin-scale stratigraphic model. Computers & Geosciences, 34, 1370–1380.

652

653   Dalman, R.A.F. and Weltje, G.J. (2012). SimClast: An aggregated forward stratigraphic model of

654   continental shelves. Computers & Geosciences, 38, 115-126.

655

656   Deutsch, C.V. (2002). Geostatistical Reservoir Modeling. Oxford University Press, Oxford, 376 p.

657

658   Edmonds, D.A. and Slingerland, R.L. (2010). Significant effect of sediment cohesion on delta

659   morphology. Nat. Geosci. 3, 105–109.

660

661   Erkens, G., Cohen, K.M., Gouw, M.J.P., Middelkoop, H. and Hoek, W.Z. (2006). Holocene sediment

662   budgets of the Rhine Delta (The Netherlands): a record of changing sediment delivery. IAHS

663   Publication, 306, 406-415.

664

665   Ester, M., Kriegel, H. P., Sander, J., and Xu, X. (1996). A density-based algorithm for discovering

666   clusters in large spatial databases with noise. In Kdd, 96(34), 226–231.

667

668   Falivene O., Frascati A., Gesbert S., Pickens J., Hsu Y., and Rovira A. (2014). Automatic calibration

669   of stratigraphic forward models for predicting reservoir presence in exploration. AAPG Bulletin, V.

670   98, No. 9 (September 2014), 1811–1835. The American Association of Petroleum Geologists. doi:

671   10.1306/02271413028.

672

673   Granjeon, D. and Joseph, P. (1999). Concepts and applications of a 3-D multiple lithology, diffusive

674   model in stratigraphic modeling. In: Harbaugh, J.W. et al. (eds.), Numerical Experiments in

675   Stratigraphy: Recent Advances in Stratigraphic and Sedimentologic Computer Simulations, SEPM

676   Special Publication 62, 197– 210.

677

678   Hijma, M.P., Cohen, K.M., 2010. Timing and magnitude of the sea-level jump preluding the

679   8200 yr event. Geology 38 (3), 275-278.

680

681   Hijma, M.P. and Cohen, K.M. (2011). Holocene transgression of the Rhine river mouth area, the

682   Netherlands/Southern North Sea: palaeogeography and sequence stratigraphy. Sedimentology, 58,

683   1453–1485.

684

685   Hijma, M.P., Cohen, K.M., Hoffmann, G., Van der Spek, A.J.F. and Stouthamer, E. (2009). From

686   river valley to estuary: the evolution of the Rhine mouth in the early to middle Holocene (western

687   Netherlands, Rhine-Meuse delta). Neth. J. Geosci., 88(1), 13–53.

688

689   Karamitopoulos, P., Weltje, G.J. and Dalman, R.A.F. (2014). Allogenic controls on autogenic

690   variability in fluvio-deltaic systems: Inferences from analysis of synthetic stratigraphy. Basin

691   Research, 26(6), 767-779. DOI: 10.1111/bre.12065.

692

693   Karssenberg, D., Tornqvist, T. and Bridge, J.S. (2001). Conditioning a process-based model of

694   sedimentary architecture to well data. Journal of Sedimentary Research 71, 868-879.

695

696   Karssenberg, D., De Vries, M. and Bridge, J.S. (2007). Conditioning a process-based fluvial-
697   stratigraphy model to well data by inverse estimation of model inputs using a genetic algorithm.
698   AAPG Search and Discovery Article #90063, AAPG Annual Convention, Long Beach, California.
699
700   Koster, K., Stafleu, J. and Cohen, K.M. (2016). Generic 3D interpolation of Holocene base-level rise
701   and provision of accommodation space, developed for the Netherlands coastal plain and infilled
702   paleovalleys. Basin Research, 1-23. doi:10.1190/1.2720496.
703
704   Imhof, M.G. and Sharma A.K. (2007). Seismostratigraphic inversion: Appraisal, ambiguity and
705   uncertainty: Geophysics, v. 72, R51–R66, doi:10.1111/bre.12202.
706
707   Imhof, M. and Sharma, A.K. (2006). Quantitative seismostratigraphic inversion of a prograding delta
708   from   seismic   data: Marine   and   Petroleum   Geology,   23,   735–744,
709   doi:10.1016/j.marpetgeo.2006.04.004.
710
711   Hampson, G.J. (2000). Discontinuity, surfaces, clinoforms, and facies architecture in a wave-
712   dominated, shoreface-shelf parasequence. Journal of Sedimentary Research, 70, 325-340.
713
714   Hajek, E.A. and Wolinsky, M.A. (2012). Simplified processmodeling of river avulsion and alluvial
715   architecture: Connecting   models   and   field   data.   Sedimentary   Geology,   257-260,   1-30.
716   https://doi.org/10.1016/j.sedgeo.2011.09.005.
717
718   Hijma, M.P. and Cohen, K.M. (2006). Timing and magnitude of the sea-level jump preluding the
719   8200 yr event. Geological Society of America, 38 (3), 275-278, doi:10.1030/G30439.1.
720
721   Maljers, D., Stafleu, J., Van der Meulen, M.J. & R.M. Dambrink (2015) Advances in Constructing
722   Regional Geological Voxel Models, Illustrated by their Application in Aggregate Resource
723   Assessments. Netherlands Journal of Geosciences. 94. p. 257-270.
724
725   Martinius, A.W., Howell, J.A., and Good, T. (2014). Sediment-Body Geometry and Heterogeneity:
726   Analogue Studies for Modelling the Subsurface. Geological Society Special Publications 387, p. 299.
727
728   Meijer, X.D. (2002). Modelling the drainage evolution of a river-shelf system forced by Quaternary
729   glacio-eustasy. Basin Research, 14, 361–377.
730
731   Mishra, S. (2006). Some new test functions for global optimization and performance of repulsive
732   particle swarm method. ACM Transactions on Modeling and Computer Simulation.

733

734 Paola, C. (2000). Quantitative models of sedimentary basin filling. Sedimentology, 47, 121–178.

735

736 Peter, C., Sacchi, Q., Serazio, C. and Verga, F. (2017). Capturing channelized reservoir connectivity

737 uncertainty with amalgamation curves. Marine and Petroleum Geology, 88, 329-342.

738 https://doi.org/10.1016/j.marpetgeo.2017.07.017.

739

740 Reynolds, A.D. (1999). Dimensions of Paralic Sandstone Bodies. In: AAPG Bulletin, 83, 211-229.

741

742 Rosenbrock, H.H. (1960). An automatic method for finding the greatest or least value of a function.

743 The Computer Journal. 3 (3): 175–184. doi:10.1093/comjnl/3.3.175. ISSN 0010-4620.

744

745 Sacchi, Q., Weltje, G.J. and Verga, F. (2015). Towards process-based modelling: Obtaining basin-

746 scale constraints from seismic and well data. Marine and Petroleum Geology, 61, 56-68.

747

748 Sacchi, Q., Borello, E.S., Weltje, G.J. and Dalman, R.A.F. (2016). Increasing the predictive power of

749 geostatistical reservoir models by integration of geological constraints from stratigraphic forward

750 modelling. Marine and Petroleum Geology, 69, 112-126.

751

752 Sambridge, M. (1999). Geophysical inversion with a neighborhood algorithm–Searching a parameters

753 space: Geophysical Journal International, 138, 479–494, doi:10.1046/j.1365-246X.1999.00876.x.

754

755 Sambridge, M. (2001). Finding acceptable models in nonlinear inverse problems using a

756 neighborhood algorithm: Inverse Problems, 17, 387–403, doi:10.1088/0266-5611/17/3/302.

757

758 Sambridge, M., and K. Mosegaard (2002). Monte Carlo methods in geophysical inverse problems:

759 Reviews of Geophysics, 40, 1–29. doi: 10.1029/2000RG000089.

760

761 Sharma, A. K. (2006). Quantitative stratigraphic inversion, Ph.D. Dissertation, Virginia Polytechnic

762 Institute and State University, Blacksburg, Virginia, 91 p.

763

764 Stafleu, J., Maljers, D., Gunnink, J.L., Menkovic, A. and Busschers, F.S. (2011). 3D modelling of the

765 shallow subsurface of Zeeland, the Netherlands. Netherlands Journal of Geosciences 90, 293–310.

766

767 Stafleu, J., Maljers, D., Busschers, F.S., Gunnink, J.L., Schokker, J., Dambrink, R.M., Hummelman,

768 H.J. & M.L. Schijf (2012) *GeoTOP modellering (in Dutch).* TNO Report TNO-2012-R10991, 216 p.

769

770 Stafleu, J. & C.W. Dubelaar (2016) Product Specification Subsurface model GeoTOP. TNO Report
771 2016 R10133 v1.3, 53 p.

773 Stafleu, J. and F.S. Busschers, 2017. Analysing lithological and grain-size trends using a 3D voxel
774 model: a case study from the Holocene Rhine-Meuse delta (Extended Abstract, 5 pp). 79th EAGE
775 Conference & Exhibition 2017 – Workshop Programme, Paris, France, 12-15 June 2017.

777 Stouthamer, E., Cohen, K.M. and Gouw, M.J.P. (2011). Avulsion and its implications for fluvial-
778 deltaic architecture: insights from the holocene rhine–meuse delta. In: From River To Rock Record:
779 The Preservation Of Fluvial Sediments And Their Subsequent Interpretation. SEPM Special
780 Publication No. 97, 215-231.

782 Styblinski, M. and Tang, T. (1990). Experiments in Nonconvex Optimization: Stochastic
783 Approximation with Function Smoothing and Simulated Annealing, Neural Networks, 3, 467-483.

785 Van der Meulen, Michiel and Doornenbal, J.C. and Gunnink, Jan and Stafleu, Jan and Schokker,
786 Jeroen and Vernes, R.W. and Geer, Frans and Gessel, S.F. and Heteren, Sytze and Leeuwen, R.J.W.
787 and Bakker, Marcel A.J. and Bogaard, Paul and Busschers, F.s and Griffioen, J. and Gruijters,
788 S.H.L.L. and Kiden, Patrick and Schroot, B.M. and Simmelink, HJ and Berkel, W.O. and Daalen,
789 T.M.. (2013). 3D geology in a 2D country: Perspectives for geological surveying in the Netherlands.
790 Netherlands Journal of Geosciences - Geologie en Mijnbouw. 92. 217-241.
791 10.1017/S0016774600000184.

793 Weltje, G.J., Dalman, R.A.F., Karamitopoulos, P., Sacchi, Q. (2013). Reducing the uncertainty of
794 static reservoir models: implementation of basin-scale geological constraints. Spe-164821-ms.

796 Wijns, C., Poulet, T., Boschetti, F., Dyt, C., Griffiths, C.M. (2004). Interactive inverse methodology
797 applied to stratigraphic forward modelling. In: Curtis, A., Wood, R. (eds.), Geological Prior
798 Information: Informing Science and Engineering. Geological Society Special Publication 239, 147-
799 156.
800